Letter

Retarded Charge Recombination to Enhance Photocatalytic Performance for Water-Free CO_2 Reduction Using Perovskite Nanocrystals as Photocatalysts

Sudhakar Narra, Sumit S. Bhosale, Aparna K. Kharade, Sue-min Chang, and Eric Wei-Guang Diau*

Read Online

ACCESS | Metrics & More | Article Recommendations | SI Supporting Information

ABSTRACT: Femtosecond transient absorption spectral (TAS) investigations were performed to understand the carrier relaxation mechanism for perovskite nanocrystals $Cs_{1-x}FA_xPbBr_3$ (CF, $x = 0.45$) and $CsPbBr_3$ (CS), which served as efficient photocatalysts for splitting of CO_2 into CO and O_2 in the absence of water. Upon light irradiation for 12 h, formation of deep trap states was found for both CS and CF samples with spectral characteristics of the TAS photobleach (PB) band showing a long spectral tail extending to the long wavelength region. The charge recombination rates at the shallow surface states, bulk states, and deep-trapped surface state were found to be significantly retarded for the CF sample than for the CS sample, in agreement with the photocatalytic performances for CO product yields of the CF catalyst being greater by a factor of 3 compared to those of the CS catalyst.
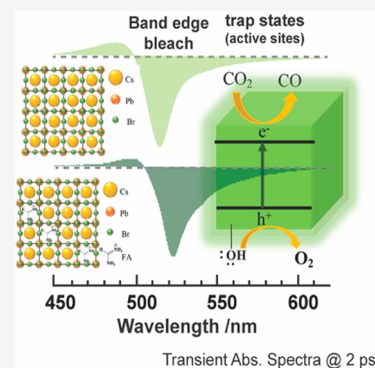
Carbon dioxide (CO_2) is a major greenhouse gas responsible for the global-warming problem.[1-3] Development of good strategies to remove CO_2 generated via human activity is thus an urgent task for scientists to pursue.[2-4] Photocatalytic reducing of CO_2 to generate CO and/or low carbon fuels becomes a popular research topic recently.[5] Among those potential photocatalysts, lead halide perovskite nanocrystals (PeNC) are emerging as promising candidates due to their advantages of feasible synthesis, great tunable optical properties, and excellent charge separation ability upon light irradiation.[6-9] For example, $CsPbBr_3$ (CS) PeNC has been widely applied for CO_2 reduction to attain great CO production yields.[9-14]

The production yields of a photocatalytic reaction depend on several critical factors such as optical bandgap, absorption coefficient, particle sizes, surface defects, and crystal structures.[7,8] For example, Hou et al.[15] showed that CS PeNC with an optimum size of 8.5 nm yielded better photocatalytic activity than smaller or larger size crystals. Shyamal et al.[16] showed that the facet and defects may affect the photocatalytic activity of CS PeNC; they concluded that CS PeNC with a noncubic structure exhibited better CO production yields than the cubic structure due to the formation of surfaces with lower adsorption energies for CO_2 chemisorption. Furthermore, they showed that the PL lifetimes of the noncubic structures were shorter than those of the cubic structures due to formation of defect sites feasible for CO_2 adsorption. Thus, tuning the crystal structure along with creation of active sites is key to boost the photocatalytic performance of CS PeNC. A site using cationic engineering

with organic cations such as methylammonium (MA) or formamidinium (FA) cations can be a good strategy to tune the crystal structures and induce more active sites on the surface of PeNC with lower activation barriers for ion migration.[17,18] Among these two organic cations, FA offers greater stability due to a slightly higher activation barrier than MA, and also it forms the more stable cationic PeNC.[17]

In the present study, we developed a noncubic PeNC by incorporating FA cation into the reference CS PeNC nanocrystal to form a cocationic PeNC, $Cs_{1-x}FA_xPbBr_3$ (CF, $x = 0.45$ determined by SEM/EDX data), synthesized using the hot addition method (HAM) developed by ourself.[19,20] We found that the CO product yield of photocatalytic CO_2 reduction using CF as a catalyst is three times greater than that using CS as a catalyst in the absence of water.[21] *In situ* femtosecond transient absorption spectral (TAS) studies for both CS and CF samples were carried out to understand the relaxation dynamics of photoinduced charge carriers for both catalysts in their pristine forms, in an N_2 environment irradiated for 12 h, and in an environment adsorbed with CO_2 irradiated for 12 h. We found that the TAS transients of photobleach (PB) bands show charge recombination in two

time scales; the rapid decay corresponds to the shallow surface trap state relaxation while the slow decay corresponds to the bulk trap state relaxation. Photoactivation of the pristine and CO_2-adsorbed films generates deep trap states with two recombination components. A new photoinduced absorption (PIA) band was involved in the CS samples, but it only appeared on CF samples after photoactivation. The observed retarded charge recombination for the CF catalyst is responsible for its superior photocatalytic performance
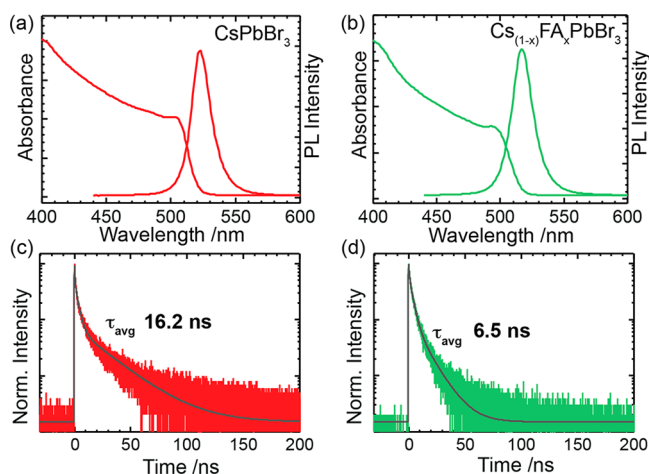
Figure 1. Absorbance, photoluminescence (PL) spectra, and PL decay profiles of (a, c) $CsPbBr_3$ and (b, d) $Cs_{1-x}FA_xPbBr_3$ as colloidal suspensions in toluene.

compared to that of the CS catalyst.[21] A relaxation mechanism is established for PeNC photocatalysts to account for their photoinduced charge recombination process that is consistent with the photocatalytic activities observed for CF and CS catalysts.

The CF PeNC was synthesized via the HAM by adding FABr/IPA solution to the reaction mixture prior to injection of Cs−oleate as reported elsewhere.[19,20] The CS PeNC was synthesized using the traditional hot-injection method[22] to compare with the HAM-synthesized CF. Figure S1 shows that both PeNCs are cubic and highly crystalline with average nanocrystal size of ∼8 nm. In addition, XRD and TOPAS results show that both PeNCs have mixed cubic and orthorhombic phases with varied proportions: the CF PeNC comprises 7% cubic and 93% orthorhombic phases whereas the CS PeNC has 38% cubic and 62% orthorhombic phases.[21] After CO_2 reduction for 12 h, both catalysts show enhance-

ment in the cubic phase from 38% to 73% for CS and 7% to 47% for CF.[21] Note that the CF catalyst contains more portions of orthorhombic phase than the CS catalyst, implying that the former may have more spaces than CS to adsorb more CO_2 molecules on the crystal surface to enhance its photocatalytic performance.

The optical properties such as absorption and emission spectra of CS and CF PeNCs as colloidal suspensions in toluene solution are similar (Figure 1, parts a and b). Both PeNCs show absorption in the 300−520 nm region with the maximum excitonic absorption at 503 and 494 nm for CS and CF, respectively; the emission peaks are located at 525 and 517 nm for CS and CF, respectively. Despite the fact that both PeNCs have very similar absorption and emission characteristics, there is a difference in PL decays. PL decay profiles were measured using a time-correlated single-photon-counting (TCSPC) system with excitation at 375 nm and probed at the PL maximum. Decay profiles for both CS and CF PeNCs in solution (Figure 1, parts c and d) were fitted with a triexponential decay function, the corresponding fitted time coefficients are listed in Table S1. CF has larger τ_1 than CS (0.6 vs 0.3 ns), indicating that the solvent-induced relaxation in the surface state is slower for CF than for CS. In contrast, much larger τ_3 was observed for CS than for CF, probably due to the contribution of the cubic phase being higher for CS than for CF, which is consistent well with the fact that shorter PL lifetimes were shown in noncubic phases than in cubic phase.[16] The *in situ* TCSPC results of the CF thin-film samples are shown in Figure 2 and Table S2, for which the PL decay profiles of pristine film without irradiation, the film in N_2 environment under light irradiation for 12 h and the CO_2-adsorbed film under light irradiation for 12 h are presented. The PL transients of the CF thin-film sample show generally slower decay feature than that of the CF solution sample due to lack of solvent-induced relaxation in the thin-film sample. After light irradiation for 12 h, the decay coefficients of the photoactivated samples are significantly larger than those of the pristine sample, and this phenomenon might be due to the effect of Ostwald ripening,[23] or the contribution of the enhanced cubic phase with longer PL lifetime than that of orthorhombic phase after photoirradiation. The CO_2-adsorbed sample shows greater PL lifetimes than those in the absence of CO_2, indicating the involvement of the CO_2 reduction to enlarge the crystal size further with better charge separation.

The CO_2 reduction experiments were carried out in the quartz reactor with a total volume of 200 mL. N_2 gas was passed for 1 h to dry the PeNC film and to remove air to ensure that the reaction system was under anaerobic
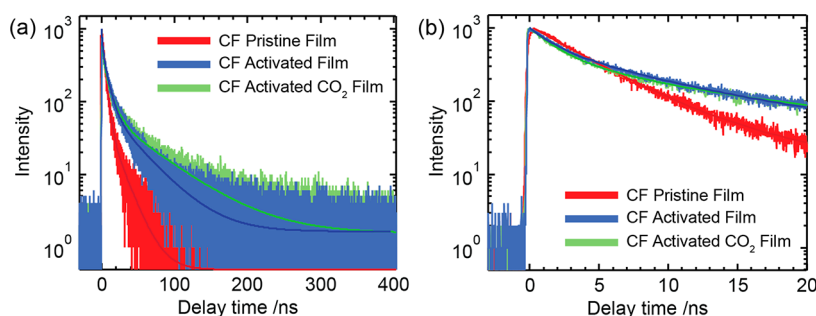
Figure 2. (a) PL transient decay profiles of the CF thin-film samples under three different conditions as indicated. (b) Expanded view of these decay profiles.
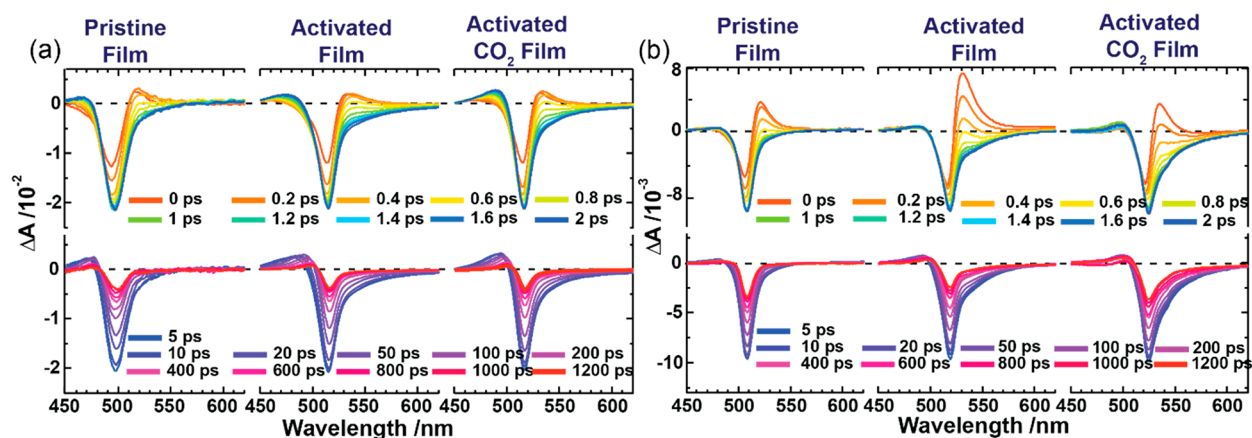
Figure 3. TAS profiles of (a) $CsPbBr_3$ (CS) and (b) $Cs_{1-x}FA_xPbBr_3$ (CF) for pristine, activated, and activated CO_2.
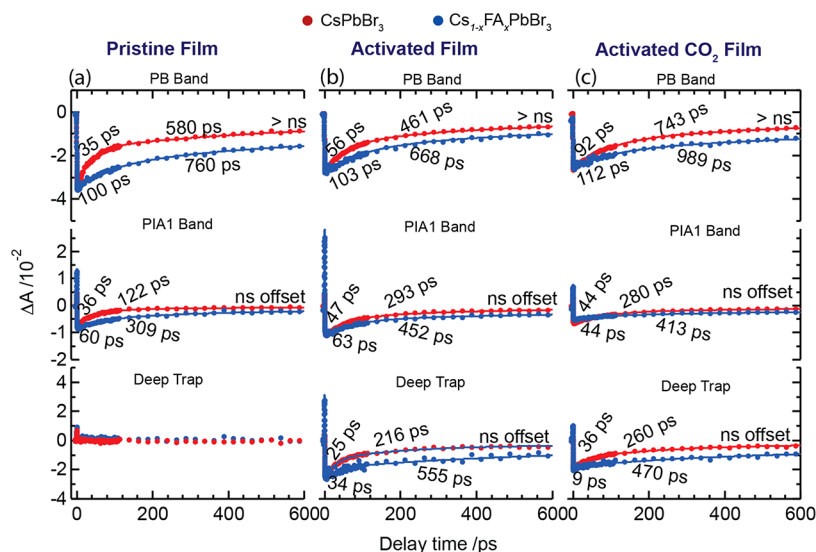

Figure 4. Transient decay profiles of the CS and CF samples monitored at the minima of the PB band, maximum of the PIA1 band, and deep trap state (570 nm) for (a) pristine film, (b) photoactivated film, and (c) CO_2-adsorbed photoactivated film.
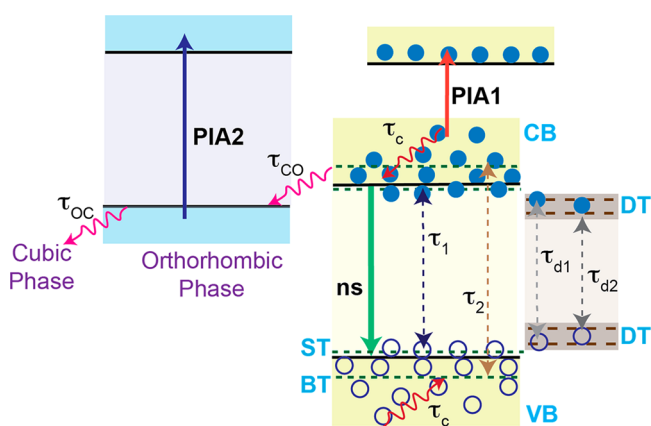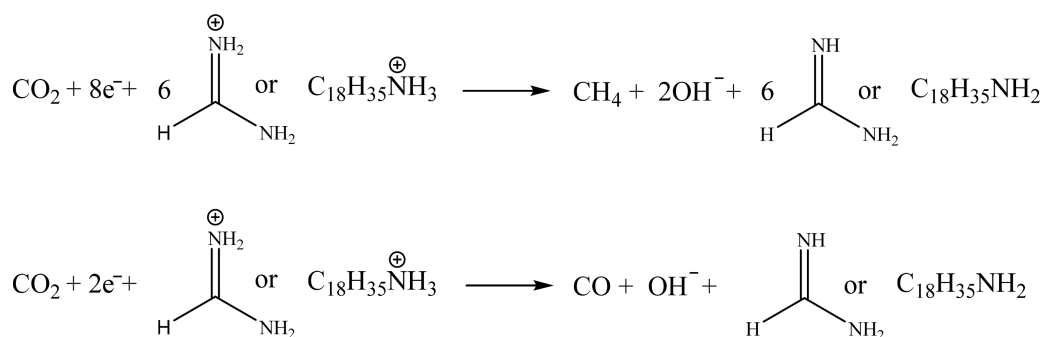

Figure 5. Relaxation mechanism of CS and CF PeNC. VB represents the valence band, CB the conduction band, BT the bulk trap states, ST the shallow trap states, and DT the deep trap states; τ_c, τ_1, τ_2, τ_{OC}, and τ_{CO} represent time coefficients for hot-carrier cooling, shallow trap state recombination, bulk trap state recombination, phase transition from cubic to orthorhombic phase and its reverse phase transition, respectively. τ_{d1}, τ_{d2} are time coefficients for sub-band gap deep trap states.

conditions. Dry CO_2 was purged in a photoreactor at 50 mL min^{-1} for 1 h to perform photocatalytic CO_2 reduction in the absence of water. A solar simulator with power 1000 W m^{-2} (one sun) was used as the light source to irradiate the samples for 12 h and the CO and methane products were analyzed using the GC-TCD and GC-FID systems, respectively. The product yields of CO for CF and CS were obtained to be 1.105 ± 0.083 vs 0.349 ± 0.036 μmol g^{-1},[21] respectively, indicating the significantly improved photocatalytic performance for the CF photocatalyst with addition of FA to serve with additional proton source for the CO_2 reduction rate to accelerate.

To understand the relaxation dynamics for the photocatalysts, *in situ* TAS studies of CS and CF PeNC samples were carried out using a fs pump pulse at 397 nm with a fs white-light probe pulse in the region between 450−650 nm for the samples in the same reactor as photocatalytic experiments under three different conditions: (i) pristine film without irradiation, (ii) N_2-filled film photoactivated under light irradiation for 12 h, and (iii) CO_2-adsorbed film under light irradiation for 12 h. The TAS profiles of the CS and CF thin-film samples are shown in parts a and b of Figure 3, respectively, and the related relaxation kinetics are shown in parts a−c of Figures 4; the corresponding fitted kinetic

Scheme 1. Chemical Equations Showing the CO_2 Reduction Using CF as a Catalyst to Produce Methane (Top) and CO (Bottom)[a]

$$CO_2 + 8e^- + 6 \;\; \overset{\oplus}{NH_2} \text{ or } C_{18}H_{35}\overset{\oplus}{NH_3} \longrightarrow CH_4 + 2OH^- + 6 \;\; NH \text{ or } C_{18}H_{35}NH_2$$

$$CO_2 + 2e^- + \;\; \overset{\oplus}{NH_2} \text{ or } C_{18}H_{35}\overset{\oplus}{NH_3} \longrightarrow CO + OH^- + \;\; NH \text{ or } C_{18}H_{35}NH_2$$

[a]The proton source came from either formamidinium or oleylammonium which can be released from CF upon irradiation.[21]

parameters are summarized in Tables S3−S5 for samples i−iii, respectively.

The PB band of the CS sample (Figure 3a) shows absorption bleach position at 497 nm, while photoactivation shifted the PB band of CS by 18 to 515 nm. Similarly, the PB band of the CF sample (Figure 3b) shows absorption bleach position at 508 nm, while photoactivation shifted the PB band by 10 to 518 nm. Furthermore, illumination of PeNCs in the presence of CO_2 produces very small spectral shift (~1 to 516 nm) for the PB band of the CS sample, but the PB band of the CF sample was red-shifted by 6 to 524 nm. The red shift of the PB band to longer wavelengths can be understood in terms of increase of particle size for nanocrystals as reported elsewhere.[24] These results are consistent with our previous results[21] for the TEM images showing the aggregated nanocrystals with larger sizes, the XRD patterns showing the sharper diffraction peaks, and the TCSPC transients (Figure 2) showing the greater PL lifetimes after light irradiation, due to the effect of Ostwald ripening and possibly the enhanced contribution of cubic phase discussed elsewhere.[21] Furthermore, we notice that both photoactivated samples of CS and CF show red tails of the PB bands which greatly extended to the 600 nm region, while the PB bands are nearly symmetrical for both pristine samples of CS and CF. This is a spectral feature showing formation of deep trap states for the photoactivated samples, as deep trap states often feature weak absorption in the sub bandgap region. In addition, the signature of the deep trap states is more pronounced for the CF sample than for the CS sample, indicating that more deep trap states were produced and involved in the photocatalytic reaction for CF than for CS. Furthermore, the lowered activation energy for the halide ion migration in the case of CF might cause the effect of cation rotation and tilts of the lead halide octahedron which is absent in the case of CS sample.[17] This is an important factor for the CF catalyst because the halide ion migration leads to formation of bromine vacancies that provide active sites for CO_2 chemisorption.

Another spectral feature of the TAS transients is the evolution of the PIA bands on the low-energy (PIA1) and high-energy (PIA2) sides of the PB bands. The PIA1 band appears at time-zero and disappears within 1 ps for all samples. In contrast, the PIA2 band was unambiguously observed for the CS samples, but it was hardly observed for the pristine sample of CF. After light irradiation of the CF samples for 12 h, the feature of the PIA2 band appears, consistent with its origin coming from the cubic phase that can be enhanced via

photoirradiation.[21] We therefore assign the evolution of the low-energy PIA1 band to be the hot carrier relaxation to the cold species[25−27] whereas the high-energy PIA2 band to be the photoinduced phase transition from cubic to orthorhombic structure.[28] The recovery feature of the transient profiles of the PB bands of both CS and CF samples shown in Figure 4a−c can be fitted with one subpicosecond rise component (zoomed views in the range 0−10 ps are shown in Figure S2), two picosecond decay components and one nanosecond offset; similarly for the PIA1 bands, the positive TAS signal was decaying within the subpicosecond scale while the negative TAS signal was recovering with two picosecond decay components together with a nanosecond offset. For the PIA2 band, only the transient profiles of the CS samples are provided (Figure S3 and Table S6) because the TAS signals of the CF samples were too weak and scattered to give a satisfactory fit. Nevertheless, the recovery kinetics of the PIA2 band of the CS samples represent the reversible transition back from orthorhombic to cubic phase, which took 300−430 ps, in accordance with those observed for time-resolved XRD measurements.[28] The PIA2 band of CS show two rise components with rising coefficients 2 and 12−14 ps for pristine and photoactivated samples due to the transition from the cubic to orthorhombic phase, but for the in situ CO_2 sample, much more rapid rise components (0.3 and 3 ps) were observed, probably due to the effect of chemisorbed CO_2 molecules on the surface of PeNC accelerating the phase transition process. As mentioned above, the pristine CF sample is predominantly orthorhombic; thus, the PIA2 bands are less predominant when they are compared with those of the CS sample. As photoactivation increased the cubic phase, the PIA2 band intensities increased due to the activation of the photoinduced phase transition for both photoactivated CF samples.

Note that the free carrier model instead of exitonic model was applied here, because the low exciton binding energies were determined for both CS and CF samples according to the Elliot model (Figure S4).[29−32] Accordingly, the transient kinetics shown for PB and PIA1 bands reflect carrier relaxation through different channels. We make the following assignment for the observed multiexponential kinetics—the rapid subpicosecond decay of the PIA1 band and subpicosecond rise of the PB band (τ_c) are due to hot-carrier thermalization, the two picosecond decays of PB bands (τ_1 and τ_2) are due to charge recombination in the surface shallow trap and bulk trap states,[33−35] respectively, while the two picosecond recovery

components of PIA1 bands (τ_{d1} and τ_{d2}) are due to charge recombination from two different deep trap sites, and the nanosecond-offset represents the genuine radiative charge recombination; a schematic charge carrier relaxation model is shown in Figure 5.

In conclusion, we found that photoactivation significantly enhances the possibility of charge separation and retards the charge recombination so that these charge carriers would have more chance to participate in the following catalytic reaction. The comparison between CS and CF samples shows that the CF samples had slower charge recombination than the CS samples for all cases as the former is synthesized as a halide-rich surface using excess halide precursor to suppress the critical Pb defects, indicating that the CF sample is more suitable than the CS sample for photocatalytic experiments. Our results indicate that photoactivation of the PeNC films would generate two types of deep trap states on the surface. When excitation of the photoactive films occurs, the photoinduced charge can oxidize bound hydroxyl species with the holes at the valence band to generate oxygen, and simultaneously, the photoinduced electrons at the conduction band can reduce CO_2 to generate CO and methane with the proton source provided by formamidinium and/or oleylammonium as shown in Scheme 1.[21] The retarded charge recombination in the bulk, the shallow trap, and the deep trap states is responsible for the greater photocatalytic performance for CF than for CS. We therefore conclude that the generation of the shallow and deep trap states on the surface with retarded charge recombination plays a key role to promote the photocatalytic performance for CO_2 reduction as shown in the present study.

ASSOCIATED CONTENT

Supporting Information

The Supporting Information is available free of charge at https://pubs.acs.org/doi/10.1021/acs.jpclett.2c02393.

> Experimental methods, Figures S1−S4 (TEM, Transient decay kinetics and UV−vis absorption spectral simulations using Elliot model) and Table S1−S6 (TCSPC and TAS decay curve-fitting results) (PDF)

> Transparent Peer Review report available (PDF)

AUTHOR INFORMATION

Corresponding Author

Eric Wei-Guang Diau − *Department of Applied Chemistry and Institute of Molecular Science, National Yang Ming Chiao Tung University, Hsinchu 300093, Taiwan; Center for Emergent Functional Matter Science, National Yang Ming Chiao Tung University, Hsinchu 300093, Taiwan;* orcid.org/0000-0001-6113-5679; Email: diau@nycu.edu.tw

Authors

Sudhakar Narra − *Department of Applied Chemistry and Institute of Molecular Science, National Yang Ming Chiao Tung University, Hsinchu 300093, Taiwan; Center for Emergent Functional Matter Science, National Yang Ming Chiao Tung University, Hsinchu 300093, Taiwan;* orcid.org/0000-0003-4893-9204

Sumit S. Bhosale − *Department of Applied Chemistry and Institute of Molecular Science, National Yang Ming Chiao Tung University, Hsinchu 300093, Taiwan*

Aparna K. Kharade − *Institute of Environmental Engineering, National Yang Ming Chiao Tung University, Hsinchu 300093, Taiwan*

Sue-min Chang − *Institute of Environmental Engineering, National Yang Ming Chiao Tung University, Hsinchu 300093, Taiwan;* orcid.org/0000-0003-3548-145X

Complete contact information is available at:
https://pubs.acs.org/10.1021/acs.jpclett.2c02393

Notes

The authors declare no competing financial interest.

REFERENCES

(1) Barros, V.; Field, C. B.; Dahe, Q.; Stocker, T. F. *Managing the Risks of Extreme Events and Disasters to Advance Climate Change Adaptation*; 2009, ix−x.

(2) Goeppert, A.; Czaun, M.; Jones, J.-P.; Surya Prakash, G. K.; Olah, G. A. Recycling of Carbon Dioxide to Methanol and Derived Products - Closing the Loop. *Chem. Soc. Rev.* 2014, 43 (23), 7995−8048.

(3) Peter, S. C. Reduction of CO_2 to Chemicals and Fuels: A Solution to Global Warming and Energy Crisis. *ACS Energy Lett.* 2018, 3 (7), 1557−1561.

(4) Wu, J.; Huang, Y.; Ye, W.; Li, Y. CO_2 Reduction: From the Electrochemical to Photochemical Approach. *Adv. Sci.* 2017, 4 (11), 1700194.

(5) Kovačič, Ž.; Likozar, B.; Huš, M. Photocatalytic CO_2 Reduction: A Review of Ab Initio Mechanism, Kinetics, and Multiscale Modeling Simulations. *ACS Catal.* 2020, 10 (24), 14984−15007.

(6) Wu, L.-Y.; Mu, Y.-F.; Guo, X.-X.; Zhang, W.; Zhang, Z.-M.; Zhang, M.; Lu, T.-B. Encapsulating Perovskite Quantum Dots in Iron-Based Metal-Organic Frameworks for Efficient Photocatalytic CO_2 Reduction. *Angew. Chem.* 2019, 58 (28), 9491−9495.

(7) Shyamal, S.; Pradhan, N. Halide Perovskite Nanocrystal Photocatalysts for CO_2 Reduction: Successes and Challenges. *J. Phys. Chem. Lett.* 2020, 11 (16), 6921−6934.

(8) Raza, M. A.; Li, F.; Que, M.; Zhu, L.; Chen, X. Photocatalytic Reduction of CO_2 by Halide Perovskites: Recent Advances and Future Perspectives. *Mater. Adv.* 2021, 2 (22), 7187−7209.

(9) Bian, H.; Li, D.; Wang, S.; Yan, J.; Liu, S. F. 2D-C_3N_4 Encapsulated Perovskite Nanocrystals for Efficient Photo-Assisted Thermocatalytic CO_2 Reduction. *Chem. Sci.* 2022, 13 (5), 1335−1341.

(10) Xu, Y.-F.; Yang, M.-Z.; Chen, B.-X.; Wang, X.-D.; Chen, H.-Y.; Kuang, D.-B.; Su, C.-Y. A $CsPbBr_3$ Perovskite Quantum Dot/Graphene Oxide Composite for Photocatalytic CO_2 Reduction. *J. Am. Chem. Soc.* 2017, 139 (16), 5660−5663.

(11) Ou, M.; Tu, W.; Yin, S.; Xing, W.; Wu, S.; Wang, H.; Wan, S.; Zhong, Q.; Xu, R. Amino-Assisted Anchoring of $CsPbBr_3$ Perovskite Quantum Dots on Porous g-C_3N_4 for Enhanced Photocatalytic CO_2 Reduction. *Angew. Chem.* 2018, 57 (41), 13570−13574.

(12) Pan, A.; Ma, X.; Huang, S.; Wu, Y.; Jia, M.; Shi, Y.; Liu, Y.; Wangyang, P.; He, L.; Liu, Y. $CsPbBr_3$ Perovskite Nanocrystal Grown on MXene Nanosheets for Enhanced Photoelectric Detection and Photocatalytic CO_2 Reduction. *J. Phys. Chem. Lett.* 2019, 10 (21), 6590−6597.

(13) Wang, J.; Wang, J.; Li, N.; Du, X.; Ma, J.; He, C.; Li, Z. Direct Z-Scheme 0D/2D Heterojunction of $CsPbBr_3$ Quantum Dots/ Bi_2WO_6 Nanosheets for Efficient Photocatalytic CO_2 Reduction. *ACS Appl. Mater. Interfaces* **2020**, *12* (28), 31477−31485.

(14) Zhang, Z.; Li, L.; Jiang, Y.; Xu, J. Step-Scheme Photocatalyst of $CsPbBr_3$ Quantum Dots/BiOBr Nanosheets for Efficient CO_2 Photoreduction. *Inorg. Chem.* **2022**, *61* (7), 3351−3360.

(15) Hou, J.; Cao, S.; Wu, Y.; Gao, Z.; Liang, F.; Sun, Y.; Lin, Z.; Sun, L. Inorganic Colloidal Perovskite Quantum Dots for Robust Solar CO_2 Reduction. *Chem. Eur. J.* **2017**, *23* (40), 9481−9485.

(16) Shyamal, S.; Dutta, S. K.; Das, T.; Sen, S.; Chakraborty, S.; Pradhan, N. Facets and Defects in Perovskite Nanocrystals for Photocatalytic CO_2 Reduction. *J. Phys. Chem. Lett.* **2020**, *11* (9), 3608−3614.

(17) Holekevi Chandrappa, M. L.; Zhu, Z.; Fenning, D. P.; Ong, S. P. Correlated Octahedral Rotation and Organic Cation Reorientation Assist Halide Ion Migration in Lead Halide Perovskites. *Chem. Mater.* **2021**, *33* (12), 4672−4678.

(18) Oranskaia, A.; Yin, J.; Bakr, O. M.; Brédas, J.-L.; Mohammed, O. F. Halogen Migration in Hybrid Perovskites: The Organic Cation Matters. *J. Phys. Chem. Lett.* **2018**, *9* (18), 5474−5480.

(19) Bhosale, S. S.; Narra, S.; Jokar, E.; Manikandan, A.; Chueh, Y.-L.; Diau, E. W.-G. Functionalized Hybrid Perovskite Nanocrystals with Organic Ligands Showing a Stable 3D/2D Core/Shell Structure for Display and Laser Applications. *J. Mater. Chem. C* **2021**, *9* (48), 17341−17348.

(20) Bhosale, S. S.; Jokar, E.; Chiang, Y.-T.; Kuan, C.-H.; Khodakarami, K.; Hosseini, Z.; Chen, F.-C.; Diau, E. W.-G. Mn-Doped Organic−Inorganic Perovskite Nanocrystals for a Flexible Luminescent Solar Concentrator. *ACS Appl. Energy Mater.* **2021**, *4* (10), 10565−10573.

(21) Bhosale, S. S.; Kharade, A. K.; Narra, S.; Chang, S.-m.; Diau, E. W.-G. Self-Photocatalytic Carbon Dioxide Splitting using Co-Cationic Perovskite Nanocrystal in Absence of Water. *SSRN* **2022**, DOI: 10.2139/ssrn.4174571.

(22) Protesescu, L.; Yakunin, S.; Bodnarchuk, M. I.; Krieg, F.; Caputo, R.; Hendon, C. H.; Yang, R. X.; Walsh, A.; Kovalenko, M. V. Nanocrystals of Cesium Lead Halide Perovskites ($CsPbX_3$, X = Cl, Br, and I): Novel Optoelectronic Materials Showing Bright Emission with Wide Color Gamut. *Nano Lett.* **2015**, *15* (6), 3692−3696.

(23) DuBose, J. T.; Christy, A.; Chakkamalayath, J.; Kamat, P. V. Transformation of Perovskite Nanoplatelets to Large Nanostructures Driven by Solvent Polarity. *ACS Mater. Lett.* **2022**, *4* (1), 93−101.

(24) Ashner, M. N.; Shulenberger, K. E.; Krieg, F.; Powers, E. R.; Kovalenko, M. V.; Bawendi, M. G.; Tisdale, W. A. Size-Dependent Biexciton Spectrum in $CsPbBr_3$ Perovskite Nanocrystals. *ACS Energy Lett.* **2019**, *4* (11), 2639−2645.

(25) Price, M. B.; Butkus, J.; Jellicoe, T. C.; Sadhanala, A.; Briane, A.; Halpert, J. E.; Broch, K.; Hodgkiss, J. M.; Friend, R. H.; Deschler, F. Hot-Carrier Cooling and Photoinduced Refractive Index Changes in Organic−Inorganic Lead Halide Perovskites. *Nat. Commun.* **2015**, *6* (1), 8420.

(26) Yumoto, G.; Tahara, H.; Kawawaki, T.; Saruyama, M.; Sato, R.; Teranishi, T.; Kanemitsu, Y. Hot Biexciton Effect on Optical Gain in $CsPbI_3$ Perovskite Nanocrystals. *J. Phys. Chem. Lett.* **2018**, *9* (9), 2222−2228.

(27) Fu, J.; Xu, Q.; Han, G.; Wu, B.; Huan, C. H. A.; Leek, M. L.; Sum, T. C. Hot Carrier Cooling Mechanisms in Halide Perovskites. *Nat. Commun.* **2017**, *8* (1), 1300.

(28) Kirschner, M. S.; Diroll, B. T.; Guo, P.; Harvey, S. M.; Helweh, W.; Flanders, N. C.; Brumberg, A.; Watkins, N. E.; Leonard, A. A.; Evans, A. M.; Wasielewski, M. R.; Dichtel, W. R.; Zhang, X.; Chen, L. X.; Schaller, R. D. Photoinduced, Reversible Phase Transitions in All-Inorganic Perovskite Nanocrystals. *Nat. Commun.* **2019**, *10* (1), 504.

(29) Elliott, R. J. Intensity of Optical Absorption by Excitons. *Phys. Rev.* **1957**, *108* (6), 1384−1389.

(30) Awasthi, K.; Du, K.-B.; Wang, C.-Y.; Tsai, C.-L.; Hamada, M.; Narra, S.; Diau, E. W.-G.; Ohta, N. Electroabsorption Studies of Multicolored Lead Halide Perovskite Nanocrystalline Solid Films. *ACS Photonics* **2018**, *5* (6), 2408−2417.

(31) Qaid, S. M. H.; Ghaithan, H. M.; Al-Asbahi, B. A.; Aldwayyan, A. S. Achieving Optical Gain of the $CsPbBr_3$ Perovskite Quantum Dots and Influence of the Variable Stripe Length Method. *ACS Omega* **2021**, *6* (8), 5297−5309.

(32) Sestu, N.; Cadelano, M.; Sarritzu, V.; Chen, F.; Marongiu, D.; Piras, R.; Mainas, M.; Quochi, F.; Saba, M.; Mura, A.; Bongiovanni, G. Absorption F-Sum Rule for the Exciton Binding Energy in Methylammonium Lead Halide Perovskites. *J. Phys. Chem. Lett.* **2015**, *6* (22), 4566−4572.

(33) Socie, E.; Vale, B. R. C.; Burgos-Caminal, A.; Moser, J. Direct Observation of Shallow Trap States in Thermal Equilibrium with Band-Edge Excitons in Strongly Confined $CsPbBr_3$ Perovskite Nanoplatelets. *Adv. Opt. Mater.* **2021**, *9* (1), 2001308.

(34) Mandal, S.; Mukherjee, S.; De, C. K.; Roy, D.; Ghosh, S.; Mandal, P. K. Extent of Shallow/Deep Trap States beyond the Conduction Band Minimum in Defect-Tolerant $CsPbBr_3$ Perovskite Quantum Dot: Control over the Degree of Charge Carrier Recombination. *J. Phys. Chem. Lett.* **2020**, *11* (5), 1702−1707.

(35) Bhosale, A. H.; Narra, S.; Bhosale, S. S.; Diau, E. W.-G. Interface-Enhanced Charge Recombination in the Heterojunction between Perovskite Nanocrystals and BiOI Nanosheets Serves as an S-Scheme Photocatalyst for CO_2 Reduction. *J. Phys. Chem. Lett.* **2022**, *13* (34), 7987−7993.